

CAN GRAVITATIONAL INFALL ENERGY LEAD TO THE OBSERVED VELOCITY DISPERSION IN DLAS?

ALEXEI O. RAZOUMOV¹, MICHAEL L. NORMAN², JASON X. PROCHASKA³, JESPER SOMMER-LARSEN^{4,5}, ARTHUR M. WOLFE², AND YI-JUNG YANG⁶

Draft version June 28, 2021

ABSTRACT

The median observed velocity width v_{90} of low-ionization species in damped Ly α systems is close to 90 km s^{-1} , with $\sim 10\%$ of all systems showing $v_{90} > 210 \text{ km s}^{-1}$ at $z = 3$. We show that a relative shortage of such high-velocity neutral gas absorbers in state-of-the-art galaxy formation models is a fundamental problem, present both in grid-based and particle-based numerical simulations. Using a series of numerical simulations of varying resolution and box size to cover a wide range of halo masses, we demonstrate that energy from gravitational infall alone is insufficient to produce the velocity dispersion observed in damped Ly α systems, nor does this dispersion arise from an implementation of star formation and feedback in our highest resolution ($\sim 45 \text{ pc}$) models, if we do not put any galactic winds into our models by hand. We argue that these numerical experiments highlight the need to separate dynamics of different components of the multiphase interstellar medium at $z = 3$.

Subject headings: galaxies: formation — galaxies: kinematics and dynamics — intergalactic medium

1. INTRODUCTION

Damped Ly-alpha absorbers (DLAs) provide us with a high-resolution probe of galaxy formation processes up to redshift $z \sim 5$, allowing us to study the neutral hydrogen distribution and kinematics of young galaxies and their surroundings on scales from several pc to several kpc, although detailed information about the spatial extent of the absorbing gas cannot be readily extracted from the observed velocity line profiles. DLAs contain a large fraction of high-redshift baryons potentially available for star formation (SF; Prochaska et al. 2005), however, their in-situ SF efficiency appears to be a factor of 20-30 lower than in the present-day galaxies of comparable gas surface density (Wolfe & Chen 2006). Even though DLAs are presumably associated with fairly compact structures, they cover about a third of the sky, so there is a high probability that a line of sight to a remote quasar will contain such an absorber. Currently, just over a 1000 such systems have been studied, and their number will undoubtedly increase in coming years⁷.

One of the unsolved long-standing puzzles in our un-

derstanding of DLAs is their large neutral gas velocity dispersion (Prochaska & Wolfe 1997). The median value of v_{90} , the velocity interval encompassing 90% of the optical depth, in absorption lines of low ions associated with cold neutral gas (such as SiII, NI, FeII, etc.) is close to 90 km s^{-1} , and 10% of all systems have $v_{90} > 210 \text{ km/s}$. Observations indicate that there is virtually no correlation between the column density N_{HI} of the absorber and its absorption line velocity width, with even lower column density systems at the DLA threshold $N_{\text{HI}} = 10^{20.3} \text{ cm}^{-2}$ demonstrating velocity widths up to 400 km s^{-1} . On the other hand, a correlation is observed between the velocity widths and metallicities of the DLAs. In fact, the correlation is remarkably tight between the equivalent width of the Si II 1526 transition (a kinematic diagnostic because the line is saturated) and gas metallicity (Prochaska et al. 2007) that shows a slope matching the local velocity/metallicity relation in dwarf galaxies (Dekel & Woo 2003). These correlations may be a consequence of a relation between the mass of the galaxies and their metallicities (Wolfe & Prochaska 1998; Ledoux et al. 2006), or an indication that feedback from SF has a direct effect on the observed velocity dispersion (Nulsen et al. 1998).

To date all DLAs exhibit metal-line absorption (Prochaska et al. 2003), and one expects that they will all show significant MgII equivalent widths. The opposite is not true; the majority of MgII-selected absorbers are not DLAs. Unlike traditional low ions, MgII traces both cold and warm neutral material, as well as warm partially photoionized gas. Recently, Murphy et al. (2007) found a correlation between metallicity and the rest-frame MgII equivalent width, suggesting a link between kinematics and the metal-enrichment history of the absorber. They stressed that the absorption-line kinematics should be viewed separately from the host galaxy kinematics, in other words, the observed velocity widths need not scale directly with the mass of the DLA-hosting halos. Bouché et al. (2006) used the cross-correlation between 1806 MgII absorbers and $\sim 250,000$ luminous red

Electronic address: razoumov@ap.smu.ca

Electronic address: mnorman@cosmos.ucsd.edu

Electronic address: xavier@ucolick.org

Electronic address: jslarsen@astro.ku.dk

Electronic address: awolfe@ucsd.edu

Electronic address: yjyang@asiaa.sinica.edu.tw

¹ Institute for Computational Astrophysics, Dept. of Astronomy & Physics, Saint Mary's University, Halifax, NS, B3H 3C3, Canada

² Department of Physics, and Center for Astrophysics and Space Sciences, University of California, San Diego, La Jolla, CA 92093-0424

³ Department of Astronomy and Astrophysics, and UCO/Lick Observatory, University of California, 1156 High Street, Santa Cruz, CA 95064

⁴ Excellence Cluster Universe, Technische Universität München, Boltzmanstr. 2, D-85748 Garching, Germany

⁵ Dark Cosmology Centre, Niels Bohr Institute, University of Copenhagen, Juliane Maries Vej 30, DK-2100 Copenhagen, Denmark

⁶ Institute of Astronomy and Astrophysics, Academia Sinica, P.O. Box 23-141, Taipei 10617, Taiwan

⁷ <http://www.ucolick.org/~xavier/SDSSDLA/>

galaxies from the Sloan Digital Sky Survey to find that the absorber halo mass is anti-correlated with the Mg II equivalent width, suggesting that at least part of the observed velocity dispersion in MgII regions is produced by supernova-driven winds and/or other feedback mechanisms which could drive cold and warm gas efficiently out of lower mass ($M_{\text{halo}} < 10^{11.5} M_{\odot}$) galaxies. On the other hand, this anti-correlation could also be interpreted as a transition from cold to shock-heated gas in more massive $\sim 10^{12.5} M_{\odot}$ halos accompanied by a drop in the cumulative cross-section of neutral clouds found in these halos (Tinker & Chen 2007).

At least for now, observational data are insufficient to find a relation between the absorbing halo mass and the velocity width v_{90} of neutral absorption in DLAs. Therefore, we should consider at least three distinct physical mechanisms which could contribute especially to the high-end tail of the DLA velocity distribution:

1) If cold clouds accreting onto massive galaxies are dense enough to survive collisional heating while falling into the hot ($\sim 10^6$ K) virialized region, they could retain a sufficiently high neutral fraction with column densities above $10^{20.3} \text{ cm}^{-2}$ (McDonald & Miralda-Escudé 1999). Note that for this mechanism to be viable, the accreting gas should be already sufficiently metal-rich, as even the most metal-poor DLAs have been found to have metallicities $Z \gtrsim -2.8$, i.e. it would imply a model in which SF was ubiquitous at some time before $z = 3$ in field galaxies of mass $10^8 - 10^{10} M_{\odot}$. In this scenario a large fraction of metals observed in DLAs was produced far from massive ($\gtrsim 10^{12} M_{\odot}$) halos where we see these metals in absorption. On the other hand, it is also possible that the low-metallicity accreting material could mix efficiently with the more metal-rich environment of the massive virialized halo.

2) Conversely, DLA kinematics could be dominated by outflow velocities of supernova-driven winds, i.e. we could see feedback directly (Nulsen et al. 1998). This hypothesis is indirectly supported by the high detected outflow velocities in Lyman-break galaxies (LBGs), the higher effective widths W_{1526} of the SiII 1526Å transition in GRB-DLAs, and the anti-correlation between the absorbing halo mass and the effective line width in MgII absorbers. It would also naturally explain the metallicity-velocity correlation, since metals should be produced in the same regions which drive the winds.

3) The apparent inefficiency of in-situ SF in DLAs, coupled with their relatively high inferred cooling rates suggests a picture in which very compact star-forming regions, perhaps associated with LBGs, illuminate much more extended neutral gas structures (Wolfe & Chen 2006). Maller et al. (2001) used a toy model of DLA absorption to show that a large covering factor of the cold gas in protogalactic clumps is consistent with observations. Moreover, numerical simulations confirm that massive halos at $z = 3$ often consist of multiple compact galaxies embedded into larger neutral clouds. Combined outflows from stellar winds and SNe in these galaxies could drive large chunks of surrounding neutral material to larger galactic radii where they could pick up a higher velocity dispersion from the local galaxy group.

Although we now have absorption data on ~ 1000 DLAs, very few groups have attempted to model DLA kinematics in recent years. Both analytical and numer-

ical models in the literature tend to rely on a velocity dispersion put in by hand, in part because of our lack of understanding of the physical processes of SF and feedback on sub-galactic scales, and in part due to numerical resolution limitations.

McDonald & Miralda-Escudé (1999) used an analytical model combining the Press-Schechter formalism with a picture of individual spherically symmetric halos consisting of multiple absorbing clouds to show that the rate of energy dissipation corresponding to the velocity dispersion of these clouds necessary to produce the observed line profiles far exceeds the rate at which energy can be supplied to these clouds by gravitational collapse and mergers of halos. They noted that a large fraction of DLAs show multiple components in absorption profiles of the low-ionization lines, and that this observation can be reproduced by a model in which the missing dissipation energy comes from supernova explosions. In fact, the energy injection rate of $1.8 \times 10^{50} \text{ ergs yr}^{-1} / (10^{12} M_{\odot})$ reproduces well the fraction of multi-component DLAs and the overall absorption line velocity width distribution with the median value of $\sim 90 \text{ km s}^{-1}$.

However, their model does not provide the physical mechanism for transferring the feedback energy to the turbulent motions in gas clouds, apart from specifying the source of this energy. In addition, it is a highly approximate model which assumes spherical exponential halos consisting of discrete neutral clouds moving with a given velocity dispersion. Moreover, the same feedback energy per unit mass is injected into all halos, independently of their mass, an assumption which probably puts too much velocity dispersion into small halos.

On the numerical front, Nagamine et al. (2007) used cosmological smoothed particle hydrodynamics (SPH) simulations coupled to a phenomenological galactic wind model to compute the rate of incidence of DLAs as a function of halo mass, galaxy apparent magnitude, and impact parameter, for a variable strength of hydrodynamical feedback. In their model, gas particles were driven out of dense SF regions by hand, by assigning a momentum in random directions. The wind mass loss rate was assumed to be twice the SF rate, and the wind carried a fixed fraction of the SN feedback energy, corresponding to the fixed wind velocities of 242 km s^{-1} (weak wind) and 484 km s^{-1} (strong wind). Depending on the strength of feedback, they found that it evacuated gas from predominantly low-mass galaxies and increased the cross-section and hence the rate of incidence of more massive galaxies. In their weak feedback model $\sim 10^{9.6} M_{\odot}$ halos contributed the most to the cross-section, whereas with strong feedback the peak shifted to $\sim 10^{11} - 10^{12} M_{\odot}$ halos, depending on numerical resolution, as feedback became more and more efficient at removing gas from low-mass systems. Although, Nagamine et al. (2007) did not analyze the velocity width statistics, one would expect to see numerous line profiles with $v_{90} > 100 \text{ km s}^{-1}$ in their models, due the increased incidence rate of massive galaxies.

The purpose of this paper is twofold. First, we test a hypothesis that the observed kinematics is driven primarily by energy coming from gravitational infall in the process of hierarchical buildup of galaxies. This is essentially an extension of the idea put forward by Haehnelt et al.

(1998) that the observed DLA line profiles are caused by a combination of random halo motions, rotation, and in-fall, coupled to the paradigm of several distinct modes of accretion onto growing proto-galaxies (Dekel & Birnboim 2006). We use the approach developed in our earlier paper (Razoumov et al. 2006, hereafter Paper I), postprocessing high resolution adaptive mesh refinement (AMR) simulations of galaxy formation with high-angular resolution radiative transfer of UV ionizing photons. We improved our algorithm in several ways including a better treatment of hydrodynamical heating during the radiative transfer stage, as well as taking into account SF and feedback. We experimented with a number of SF models, including the standard four-criterion model of Cen & Ostriker (1992) and the two-mode SF model of Sommer-Larsen et al. (2003), both of which can be tuned to give the observed SF rates in the absence of or with mild feedback. Including strong feedback in our experience tends to always suppress an ongoing SF, either unless relevant scales in the clumpy interstellar medium (ISM) are resolved, or interaction between the wind and the ambient medium has been turned off.

It is well known that without any special treatment the feedback energy is quickly lost away in cooling. Several prescriptions have been suggested to alleviate this problem; popular algorithms used in particle-based galaxy formation models are (1) turning off cooling of gas particles in the feedback regions (Thacker & Couchman 2000; Sommer-Larsen et al. 2003; Stinson et al. 2006) and (2) using a subresolution model for the multiphase ISM (Springel & Hernquist 2003; Nagamine et al. 2007) usually coupled with kinematic feedback in which individual multiphase gas particles are driven out of the star-forming regions in random or specified directions.

Grid-based AMR simulations in which feedback energy is simply converted into the gas thermal energy seem to be quite effective in limiting SF, although this efficiency certainly depends on numerical and temporal resolution. In the grid-based simulations presented in Section 2 we do not suppress cooling or use any kinematic outflow model, in other words, we enforce a fairly conservative approximation to the role of SF in DLA kinematics, largely limited to conversion of some fraction of gas into stars.

In the second half of this paper (Sec. 3) we examine DLA kinematics with TreeSPH models in which radiative cooling is suppressed in regions surrounding active SF sites.

2. GRID-BASED AMR MODELS

To accumulate the absorption line statistics, in order to compare models to observations, we need to analyze a large cosmological volume, at the same time attempting to resolve clumpy gas distribution in individual galaxies. To achieve the necessary dynamical range, we use the grid-based AMR cosmological structure formation code Enzo, running a series of models with box sizes of $4h^{-1}$, $8h^{-1}$, $16h^{-1}$ and $32h^{-1}$ comoving Mpc, listed in Table 1. All of our models have the base grid size of 128^3 , with up to seven additional levels of refinement everywhere in the volume. Each level of refinement features twice the spatial and 8 times the mass resolution of the previous level. In order to check resolution effects, for each box size we also ran one 64^3 base grid model with up to seven

TABLE 1
SIMULATION PARAMETERS.

model	box comoving Mpc/h	resolution base ³ + nested+AMR
N0	4	$64^3 + 7$
N1	4	$128^3 + 7$
M0	8	$64^3 + 7$
M1	8	$128^3 + 7$
L0	16	$64^3 + 7$
L1	16	$128^3 + 7$
H0	32	$64^3 + 7$
H1	32	$128^3 + 7$
HN	32	$128^3 + 2 + 7$

levels of AMR. In addition, we ran a high-resolution simulation HN of the most massive halo in the $32h^{-1}$ Mpc model H1. For this model we traced the positions of all dark matter (DM) particles found at $z = 3$ inside the spheres of radii $2h^{-1}$ Mpc and $4h^{-1}$ Mpc centered on the target halo back to the initial redshift $z = 99$, and regenerated the initial conditions (ICs) with 2X the grid and 8X the mass resolution inside the region which contributed all DM particles to the $4h^{-1}$ Mpc sphere, and with 4X the grid resolution and 64X the mass resolution inside the region which contributed the DM particles to the $2h^{-1}$ Mpc sphere. Since the base grid resolution in this run is 128^3 , the effective resolution for the halo is 512^3 , with 7 additional levels of AMR, resulting in the same physical (200 pc) and mass resolution as the entire $8h^{-1}$ Mpc volume in model M1.

Star formation was modeled with discrete stellar particles using the prescription of Cen & Ostriker (1992), with the overdensity threshold $\delta_{\text{cr}} = 100$, the star formation efficiency $\epsilon_{\text{sf}} = 0.1$, and the stellar particle mass $M_* = 10^6 M_{\odot}$. Whenever the conditions for SF were met and there was enough gas in a cell to form at least one stellar particle, this gas was converted into stars. Although a stellar particle was created instantaneously, the actual star formation and feedback was modeled on the local dynamical timescale. At each timestep, a $\epsilon_{\text{th}} = 10^{-5}$ fraction of the rest-mass energy of the stars produced during that time interval was injected locally as thermal energy.

2.1. UVB radiative transfer

Our galaxy formation models include a non-equilibrium ionization network for hydrogen and helium, in the presence of a uniform Madau et al. (1999) UVB. The output of these simulations at $z = 3$ is then postprocessed iteratively with the UVB radiative transfer code FTTE (Razoumov & Cardall 2005) developed for nested grids, until an equilibrium position of hydrogen and helium ionization fronts is found, with the angular resolution of 192 bins over the 4π sphere, using the same UVB as in the hydrodynamical run. This algorithm is similar to the one we used in Paper I, but with an improved treatment of hydrodynamical heating. In Paper I we added a location-specific hydrodynamical heating term which would keep the temperature of each cell constant during the iterative radiative transfer stage by exactly balancing radiative cooling, provided that the radiation field in that cell stays the same as in the hy-

drodynamical calculation. Recently we found that due to numerical instabilities this approach had a tendency to overestimate the neutral fraction in the shock-heated regions of very massive halos where the radiative cooling timescale is very long. Now we simply do not update temperature in shock heated regions with $T > T_{\text{cr}}$, where $T_{\text{cr}} = 3 \times 10^4$ K. Although heating by active galactic nuclei via helium photoionization could take the temperature above 3×10^4 K, in practice we found that our results are not sensitive to the exact choice of T_{cr} , as long as it stays in the $2 \times 10^4 - 5 \times 10^4$ K range, since shock-heated regions have fairly narrow boundaries.

2.2. Spectrum generation

To generate and process artificial spectra, we follow the procedure outlined in Paper I, with one important modification. The principal line width diagnostic used throughout this paper is the velocity interval v_{90} encompassing 90% of the optical depth in the line. This diagnostic is dominated by clouds with large optical depths – its more detailed discussion and the comparison to the equivalent width can be found, e.g., in Prochaska et al. (2007). To measure v_{90} , we need an unsaturated line which also has a sufficient oscillator strength to stand out above the noise. In observations such a line is picked by hand from a set of low ionization lines associated with the absorber. In numerical models we deal with a very large number of sightlines to accumulate the statistics and therefore need a robust algorithm to pick up the suitable line automatically. One solution is to adjust the line strength by hand, so that the optical depth in the line center is always $\tau_c \sim 2 - 3$. Here we simply compute v_{90} prior to applying the noise to the spectrum. This approach nevertheless gives us the right measurement since v_{90} is not sensitive to the choice of the specific line provided that all of its components can be seen above the noise.

2.3. Results from AMR models

Figure 1 provides a quick glance at our results. The top panels show the HI column density frequency distribution $f(N, X)$ defined such that $f(N, X)dNdX$ is the number of DLAs in the intervals $[N, N + dN]$ and $[X, X + dX]$, where N is the HI column density, and dX is the “absorption distance” interval

$$dX = \frac{H_0}{H(z)}(1+z)^2 dz. \quad (1)$$

The bottom panels of Figure 1 show the line density $\ell_{\text{DLA}}(X)$, i.e. the number of DLAs per unit absorption distance with the velocity width higher than v_{90} , for $64^3 + 7$ (on the left) and $128^3 + 7$ (on the right) models, respectively. Figure 1 gives the same distributions as Figures 4 and 5 in Paper I, with several differences. First, our latest models use consistently higher grid resolution, across the wider range of volumes from $4h^{-1}$ to $32h^{-1}$ Mpc. Next, we calculate the neutral hydrogen fraction in shock-heated regions more accurately. Finally, we account for conversion of gas into stars, as well as feedback, albeit in a conservative form. Only model M1 has the same grid and mass resolution as one of the runs (C2) in Paper I, however, the above-mentioned

changes yield slightly lower HI column densities across the entire N_{HI} range.

At low column densities ($10^{20.3} - 10^{20.6} \text{ cm}^{-2}$) we find fewer absorbers than observed, with the maximum discrepancy factor of ~ 1.6 at the DLA threshold. Part of this discrepancy may be explained by a Malmquist bias in the observational result (O’Meara et al. 2007). On the other hand, our models produce consistently more high-column density absorbers, missing the turn-off at $N_{\text{HI}} \gtrsim 10^{21.5} \text{ cm}^{-2}$. This behaviour is not surprising as (1) we do not include the formation of H_2 molecules on dust grains, which is believed to be the major sink for neutral hydrogen atoms at higher densities, and (2) we do not account for gas clumping on scales below 100 pc. Apart from the uncertainties of H_2 formation at non-zero metallicities, putting this physics in by hand into our current models is not yet practical, as we do not resolve the $\sim 1 - 10$ pc scale of individual cold clouds in which these molecules form. Note that $N_{\text{HI}} = 10^{21} \text{ cm}^{-2} \approx 8 M_{\odot} \text{ pc}^{-2}$ is also a critical surface density threshold for the formation of the cold phase (e.g., Schaye 2004). Our limited numerical resolution in effect prevents conversion of gas into the cold phase which would otherwise trigger gravitational instability, i.e. further collapse of densest cores leading to much smaller cross-sections. In addition, once the multi-phase medium develops, hydrodynamical feedback from OB winds and supernovae in such a clumpy medium is likely to lead to compression of HI regions into thinner shells again producing lower cross-sections. Gas clumping on these small scales is expected to lower the rate of incidence of clouds forming H_2 which probably explains why the observed transition between the HI and H_2 column density distributions at $z = 0$ (Zwaan & Prochaska 2006) corresponds to fewer absorbers ($\log f(N, X) \sim -26$ at $N_{\text{HI}} = 10^{22} \text{ cm}^{-2}$) than what is predicted in our current models ($\log f(N, X) \sim -24.5$ at $N_{\text{HI}} = 10^{22} \text{ cm}^{-2}$).

We see the same trend found in Paper I that higher grid resolution partially alleviates the kinematics problem producing a larger fraction of $v_{90} \gtrsim 70 \text{ km s}^{-1}$ absorbers. However, the median value of v_{90} in the resolved models N1, M1 and L1 ranges from 39 to 53 km s^{-1} , well below the observed value of 90 km s^{-1} . In model H1 the median v_{90} is 64 km s^{-1} , but this model is clearly not resolved as it misses a large fraction of absorbers with $M_{\text{halo}} \lesssim 10^{11} M_{\odot}$ (Fig. 2). Similarly, going to larger computational volumes at a fixed grid and mass resolution (Fig. 3) accounts for progressively more massive halos and in smaller boxes tends to produce a larger fraction of high-velocity systems. The low median value of v_{90} is further illustrated in the HI column density vs. velocity scatter plot (Fig. 4) in which we compare a quasi-random sample of 135 observed DLAs to a sample of 135 systems picked randomly from each model.

Let us now look at how halos of different masses contribute to the overall kinematics. Figure 5 shows the v_{90} velocity widths for those DLA sightlines which pass through the virial radii of all DM halos in each model. These DLAs do not encompass our entire simulated sample, as we see a substantial fraction of $N_{\text{HI}} > 2 \times 10^{20} \text{ cm}^{-2}$ systems in filaments or intergalactic neutral clouds not associated with any particular DM halo (Table 2). This fraction varies with resolution and box size

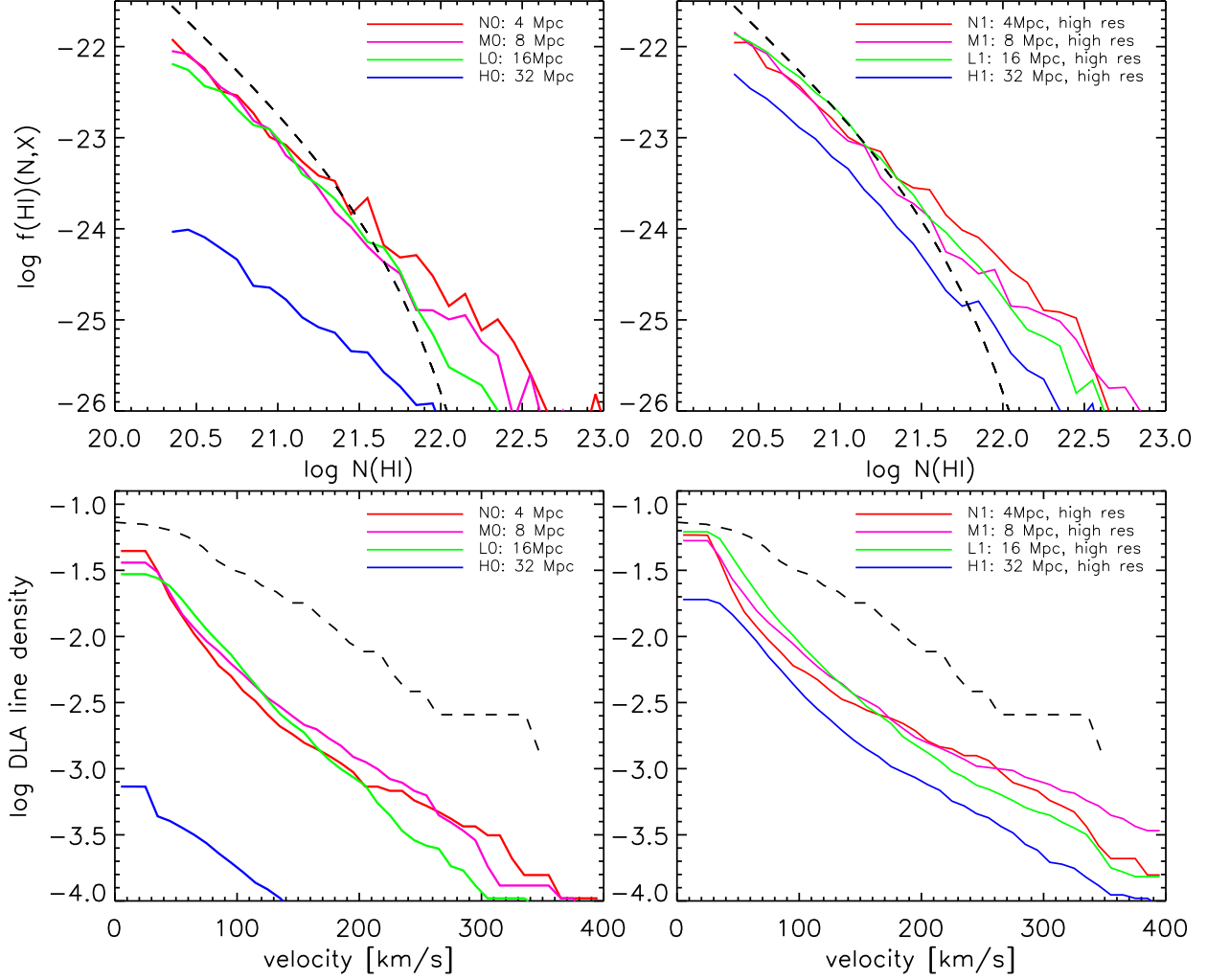


FIG. 1.— HI column density frequency distribution $f(N, X)$ (top panels, see text for details) and line density $\ell_{\text{DLA}}(X)$ of DLAs with the Si II velocity width higher than v_{SiII} vs. v_{SiII} (lower panels) for $4h^{-1}$ Mpc (red lines), $8h^{-1}$ Mpc (magenta lines), $16h^{-1}$ Mpc (green lines) and $32h^{-1}$ Mpc (blue lines) models, at $z = 3$. The panels on the left are for the $64^3 + 7$ (i.e., 7 additional levels of refinement) models, the panels on the right are for the higher resolution $128^3 + 7$ models. The dashed lines are fits to the observed distributions at $z = 3$ (Prochaska et al. 2005).

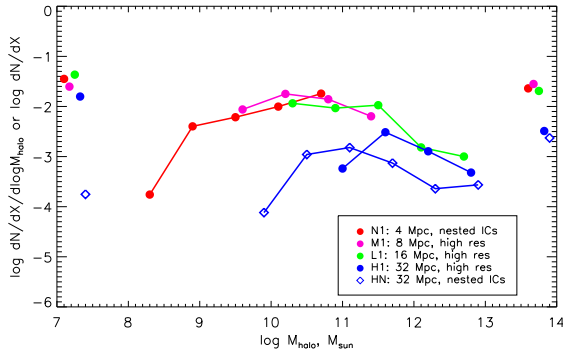


FIG. 2.— Connected points show the differential line density $dN/(dXd \log M_{\text{halo}})$ of DLAs as a function of halo mass. Isolated points on the left ($M_{\text{halo}} < 10^{7.4} M_{\odot}$) and on the right ($M_{\text{halo}} > 10^{13.6} M_{\odot}$) show the cumulative line density dN/dX of intergalactic and halo DLAs, respectively.

but is fairly large in all models, except for the nested ICs simulation of the massive halo HN in which there are very

few intergalactic DLAs. Most of the volume in this model is not resolved to have DLA-type absorption, except for the 2 Mpc refined region. This region corresponds to a higher density peak in the initial density distribution in which structures started to form earlier, with less gas left over in the diffuse filamentary form, which explains its very high fraction of DLAs associated with halos (93%).

Note that at much higher numerical resolution a lot of these intergalactic absorbers would accrete onto low-mass halos or form more compact filamentary structures with a smaller overall cross-section, so that the values given in Table 2 should probably be regarded as upper limits to the average fraction of intergalactic DLAs at $z = 3$.

The scatter in Figure 5 is quite large. Apart from the resolution effects, there is a correlation between the observed median v_{90} and the circular velocity, although this dependence has a flatter slope than the $v_{\text{obs}} \sim 0.6v_{\text{circ}}$ found by Haehnelt et al. (1998). Moreover, we see that this relation might break at higher masses where individual halos consist of multiple components, and unless

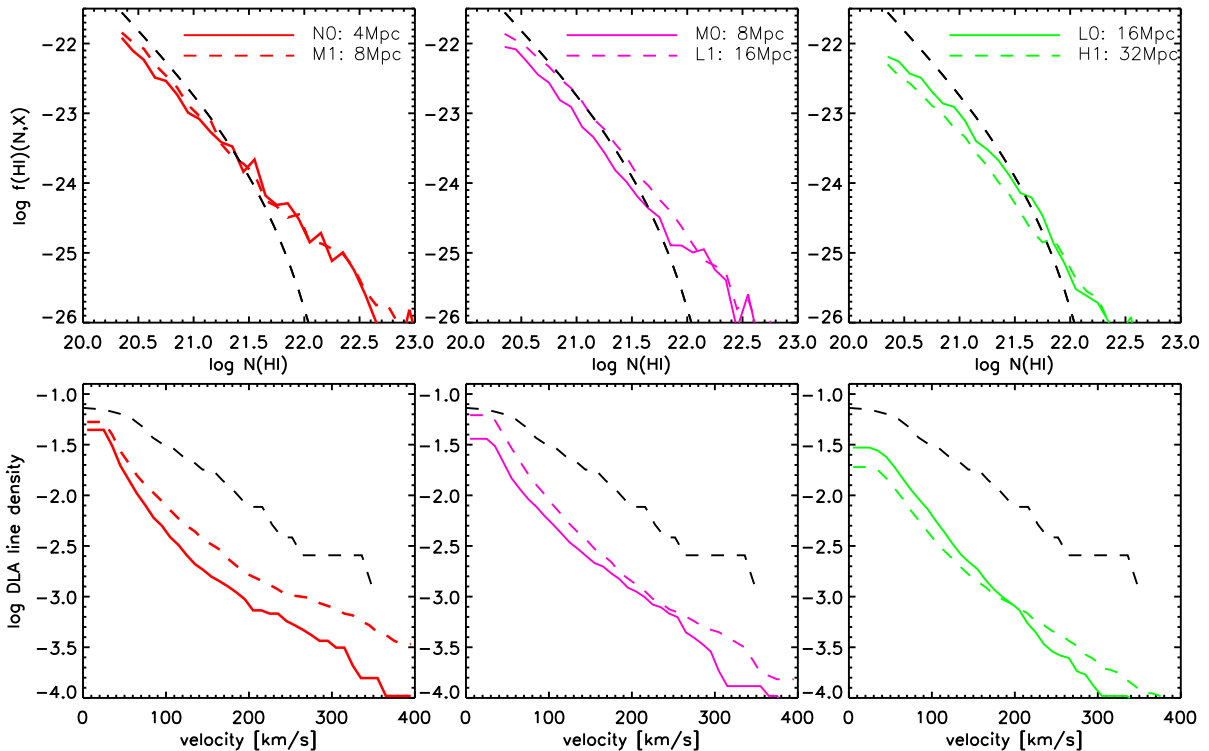


FIG. 3.— Same as Fig. 1 except that now each panel shows two simulations of same grid and mass resolution but different volumes.

TABLE 2
FRACTION OF INTERGALACTIC DLAS.

box, Mpc/h	low res	high res	nested
4	44.2%	57.6%	
8	49.7%	39.6%	
16	43.9%	54.8%	
32	26.0%	62.8%	7.0%

these components are resolved the median of the observed velocity widths can be as small as $\sim 0.2v_{\text{circ}}$.

In the top panel of Figure 6 we plotted the mass-weighted gas temperature

$$\langle T \rangle_{\text{bin}} = \int T \rho dV / \int \rho dV \quad (2)$$

averaged over the virial spheres of all halos in a given mass bin, as a function of that mass. Only halos containing at least 100 DM particles are included. It is evident that a significant fraction of the gas fails to heat to the virial temperature, since its cooling is fairly efficient and the infall velocities are relatively small. This result was first pointed out by Binney (1977) and more recently by Birnboim & Dekel (2003), who showed that in one-dimensional models a virial shock does not develop in halos below some redshift-dependent critical mass.

We find that in nested grid models lower-mass halos have the mean temperature well above their virial temperature (Fig. 6) indicating that they are found close to the virial radii of more massive halos and are being heated by the gas falling into the potential wells of their massive neighbors. A fit to all halos with $T < T_{\text{vir}}$, i.e. halos not affected by this ram-pressure heating, produces

a relationship

$$\log \langle T \rangle_{\text{bin}} = -3.51 + 0.80 \log M_{\text{halo}}, \quad (3)$$

which has a steeper slope than that of the virial temperature ($2/3$). This result can be also demonstrated by the mass fraction f_c of gas at $T < 10^4$ K (Fig. 6). Due to shock heating this fraction decreases with increasing halo mass, but in lower-mass ($10^9 \lesssim M_{\text{halo}} \lesssim 10^{11} M_{\odot}$) systems most gas can be actually found in the cold phase. As expected, the fraction f_c traces the amount of neutral gas in halos, as can be seen from the lower panel of Figure 6, where we plotted the ratio of the mass-weighted neutral fraction

$$\langle x_{\text{neu}} \rangle_{\text{bin}} = \int \frac{n_{\text{HI}} \rho dV}{n_{\text{HI}} + n_{\text{HII}}} / \int \rho dV. \quad (4)$$

to f_c . In order to explain DLA kinematics with large velocity widths of low-ionization species, we need a sufficiently large cold fraction f_c of gas in massive halos which have a high velocity dispersion. On the other hand, it is expected that halos above a certain mass scale may not contribute significantly to the observed neutral gas absorption due to shock heating of their baryons (Tinker & Chen 2007). Therefore, our goal is to determine precisely the fraction of cold gas inside compact clouds and/or accretion filaments which survive shock heating while falling into the massive halos. To have a large velocity dispersion, we need to maximize the number of such clouds intersected by any single line of sight going through the halo. In our simulations as much as $\sim 20\%$ of all gas in $10^{12} - 10^{12.5} M_{\odot}$ halos is at $T < 10^4$ K (Fig. 6), however, this amount of cold material does not automat-

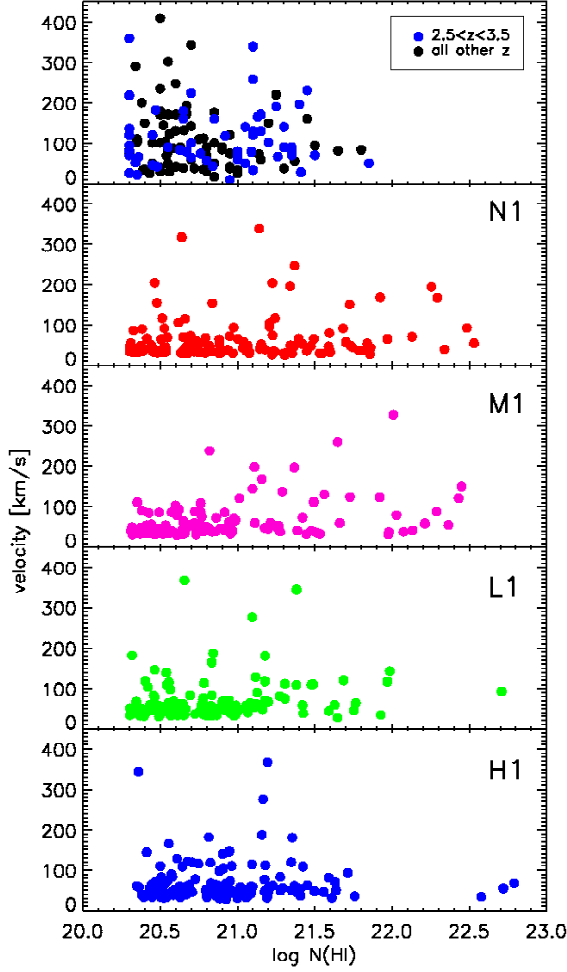


FIG. 4.— HI column density vs. velocity scatter plot for a sample of 135 observed DLAs from the SDSS DLA survey (Prochaska et al. 2005, top panel) and for 135 randomly picked DLAs from models N1, M1, L1 and H1.

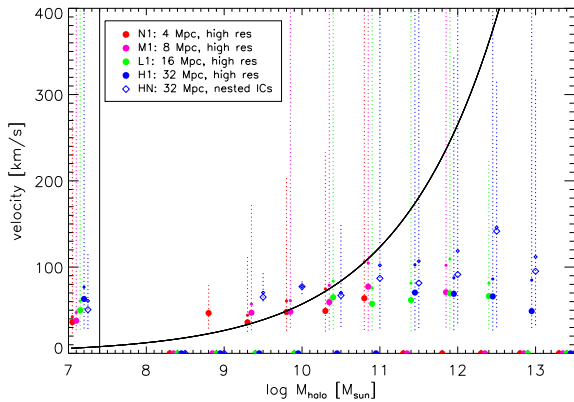


FIG. 5.— Median (large symbols) and mean (small symbols) v_{90} velocity widths for DLA sightlines which pass through virial radii of DM halos with $M_{\text{halo}} > 10^8 M_{\odot}$, vs. M_{halo} , in models S1 (red filled circles), M1 (magenta filled circles), L1 (green filled circles), H1 (blue filled circles) and HN (blue open diamonds). Dotted lines show the full range of absorption velocities in each mass bin, separately for each model. The thick solid line is the $z=3$ circular velocity. Data points on the left ($M_{\text{halo}} < 10^{7.3} M_{\odot}$) show the velocity widths for intergalactic DLAs, i.e. absorbers not associated with any halo.

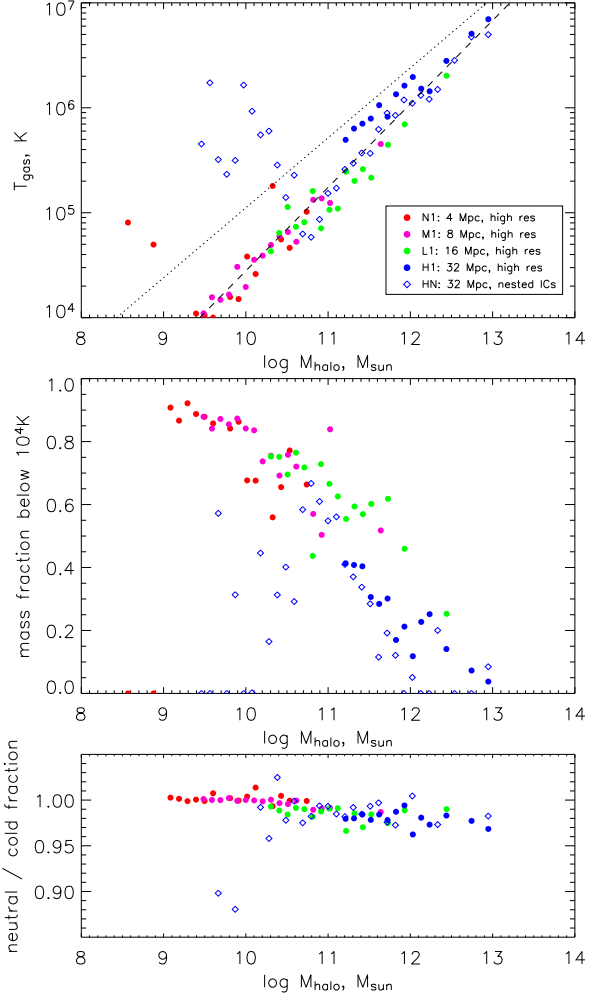


FIG. 6.— Mass-weighted average gas temperature (top panel), fraction of cold ($T < 10^4$ K) gas (center panel), and ratio of the mass-weighted average hydrogen neutral fraction to the fraction of cold gas (lower panel) inside virial radii of all halos in a given mass bin, vs. that mass, for model S1 (red filled circles), M1 (magenta filled circles), L1 (green filled circles), H1 (blue filled circles) and HN (blue open diamonds). The dotted line in the top panel shows the virial temperature at $z = 3$, while the dashed line shows the fit with Eq. 3. Note the data points above this line, indicating gas heating in small halos by larger scale dynamics in the vicinity of more massive halos.

ically produce the observed velocity dispersion.

One can argue that the spatial distribution of neutral clouds inside collapsed halos is equally important for probing the velocity space. Could improved numerical resolution change this distribution? Without running higher resolution models of isolated galaxies and understanding the physics of feedback on the scale of typical neutral structures in the ISM of absorber galaxies, it is very difficult to extrapolate our results to higher resolution. Even in our current models resolution effects show up in several different ways. First of all, in more massive ($\gtrsim 10^{11} M_{\odot}$) halos high mass resolution assists early collapse onto a larger number of low-mass DM clumps, as opposed to slower accretion via filamentary flows onto more massive and more centrally concentrated DM halos at somewhat lower redshifts (Fig. 7). Higher grid resolution leads to more efficient cooling and in general more compact shock heated regions, resulting in a higher sur-

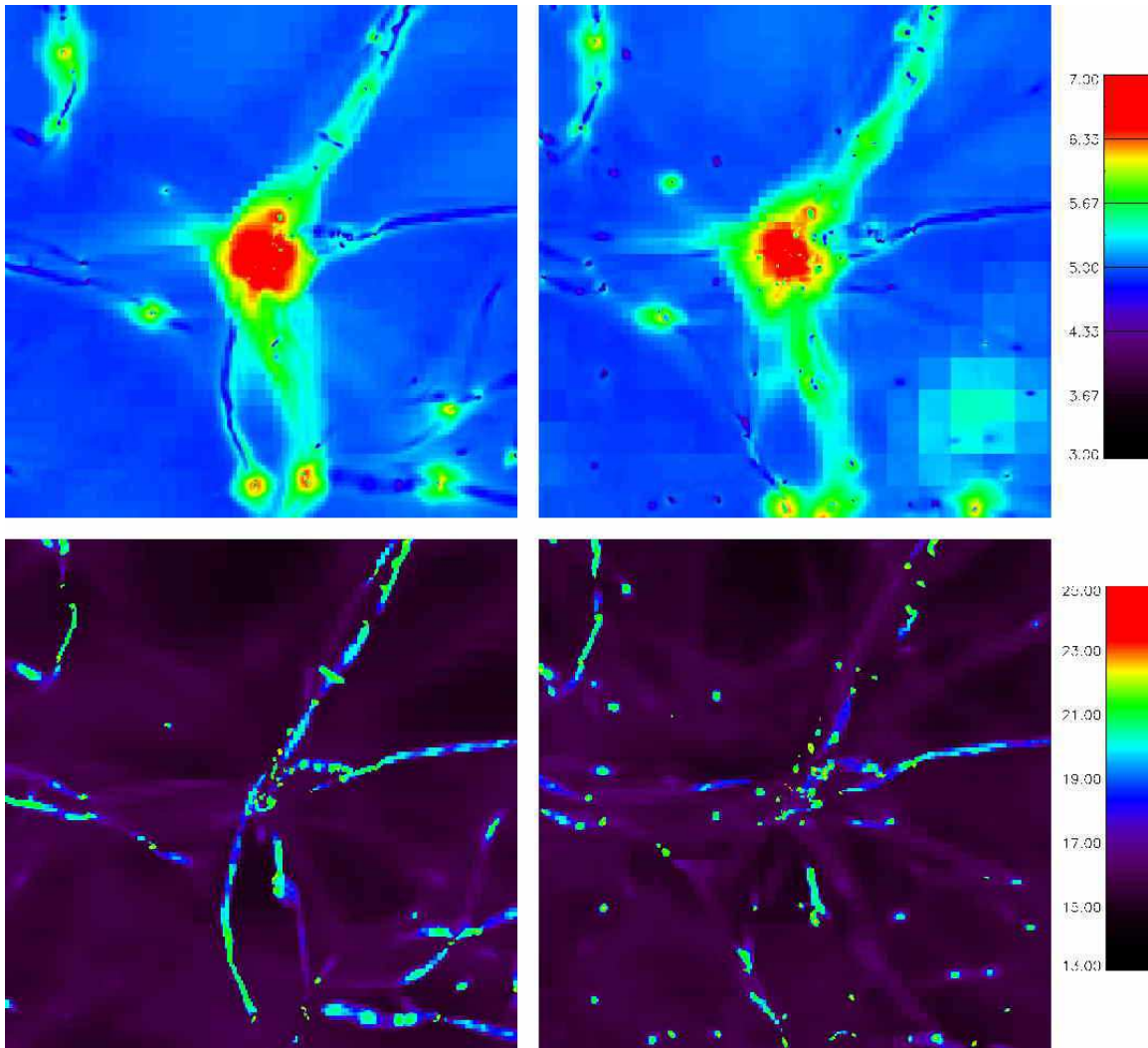


FIG. 7.— Mass-weighted temperature projection (top panels, in K) and HI column density (lower panels, in cm^{-2}) for the most massive halo ($8 \times 10^{12} M_{\odot}$) in models H1 (refined to the same $l_{\text{max}} = 7$ everywhere in the volume; left panels) and HN (the halo at the center was resimulated at 4X the highest grid and 64X the highest mass resolution of H1; right panels). Each panel is $4h^{-1}$ Mpc (comoving) on a side and $4h^{-1}$ Mpc thick.

vival probability of neutral clouds falling on massive virialized halos. The combined effect of higher mass and grid resolution in massive environments is the increased line-of-sight velocity dispersion in a larger number of compact ($\lesssim 10$ kpc) neutral gas clouds, as several of these clouds can be normally intersected by a line of sight going through such a halo. The resulting spectra feature multiple components and the combined velocity widths of up to 300 km s^{-1} (Fig. 8), with a median v_{90} value close to 90 km s^{-1} (Fig. 5).

On the other hand, in lower-mass environments, such as isolated $\lesssim 10^{10} M_{\odot}$ halos and filaments, higher numerical resolution yields a more numerous halo population, and consequently, many more neutral clouds. These clouds are sufficiently isolated so that very few of them fall on the same line of sight, and the velocity dispersion in individual clouds is too small to contribute to the large observed velocity tail, independently of resolution. However, these lower-mass environments supply the majority of low v_{90} absorbers and are an important contributor to the overall column density distribution.

Ideally, to combine the benefits of models of different volumes and resolutions, one would like to convolve the incidence rates in Figure 2 with the velocity distributions from Figure 5, using the best resolved halos in each mass bin in both distributions and adding intergalactic DLAs. Note that our 4 – 8 Mpc models represent fairly small volumes and are therefore subject to the large cosmic variance. Unfortunately, these small volumes are also the most expensive to compute, as they start to resolve the ISM, and the fraction of the volume which is refined adaptively rises steeply.

3. SPH MODELS WITH EFFICIENT FEEDBACK

We now turn to high-resolution galaxy formation models computed with the TreeSPH code (Sommer-Larsen et al. 2003) which, unlike Enzo, uses particle representation of the fluid. SF is similarly modeled with a set of discrete star particles which represent a population of stars born at the same time. Two distinct modes of SF depending on the thermal history of the star-forming gas are used: (1) early and very efficient ($\epsilon_{\text{sf}} = 1$) SF from gas which has always been cooler than

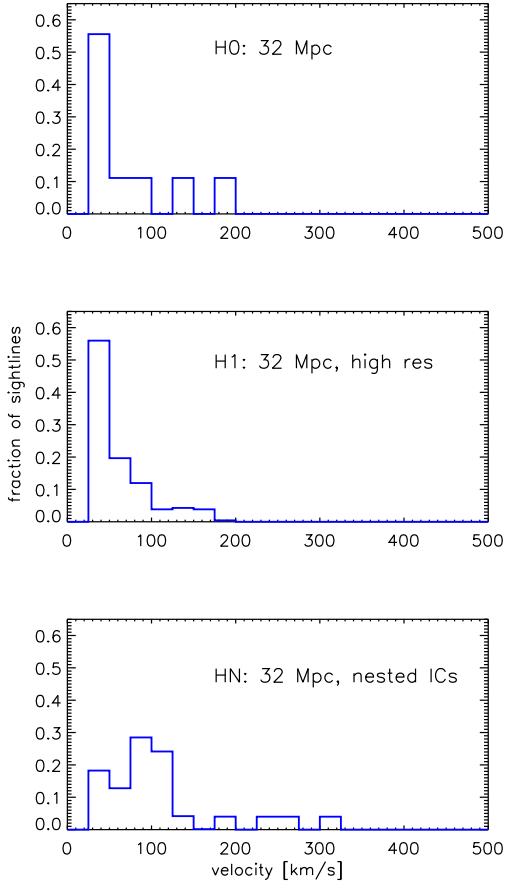


FIG. 8.— Distribution of velocity widths along random sightlines crossing the most massive halo ($8 \times 10^{12} M_{\odot}$) in $32h^{-1}$ Mpc models, at three different resolutions.

$T_{\text{cr}} = 3 \times 10^4$ K and is found above a critical density $n_{\text{H,cr}} = 0.3 \text{ cm}^{-3}$, and (2) a late mode with much lower efficiency ($\epsilon_{\text{sf}} = 5 \times 10^{-3}$) fueled by gas which has been heated to temperatures above T_{cr} and has subsequently cooled down to be found in clouds with density above $n_{\text{H,cr}} = 0.01 \text{ cm}^{-3}$.

For our purposes the most important difference between the two codes lies in implementation of feedback. In Enzo feedback energy is injected into the thermal energy of the ISM which is then allowed to be radiated away on a cooling timescale resulting in a very conservative realization of feedback. In the TreeSPH code feedback is modeled in accordance with a given initial mass function (IMF), however, cooling is suppressed in the feedback regions for the duration of the starburst, resulting in a much more efficient expansion of the heated gas into the surrounding medium. This latter approach has been shown to preserve a larger fraction of angular momentum in the baryonic component as it settles into rotationally supported disks, and to lead to more realistic disks at $z = 0$ (Sommer-Larsen et al. 2003). Can these state-of-the-art models reproduce the observed DLA kinematics at $z = 3$?

To address this question, we selected three halos from a dark matter-only run of box length $10h^{-1}$ Mpc which was then resimulated with the TreeSPH code at higher resolution in Lagrangian regions enclosing the galaxies,

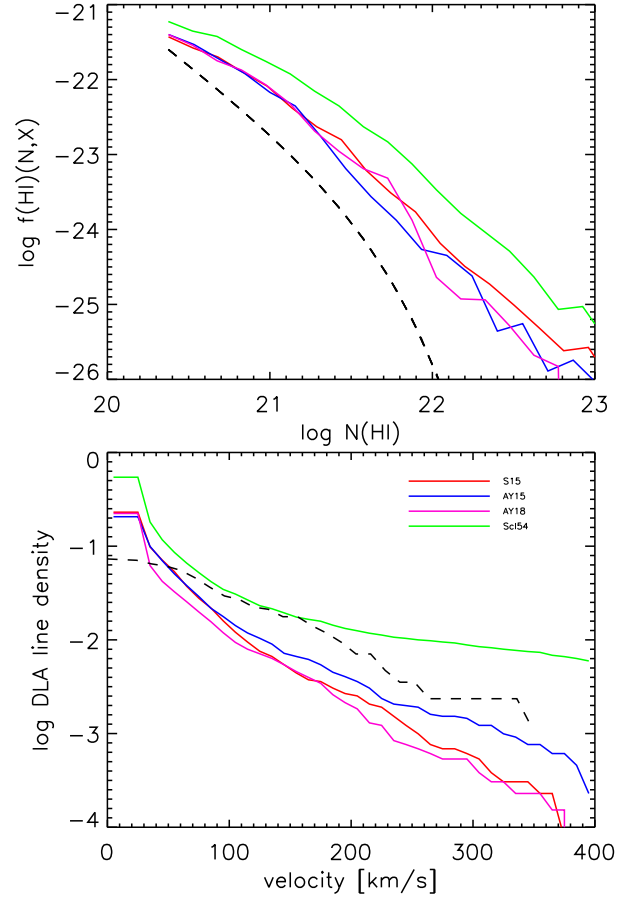


FIG. 9.— HI column density frequency distribution $f(N, X)$ (top panels) and line density $\ell_{\text{DLA}}(X)$ of DLAs with the Si II velocity width higher than v_{SiII} vs. v_{SiII} (lower panels) for the two Salpeter (S15 and Scl54) and two Arimoto-Yoshii (AY15 and AY18) models computed with the TreeSPH code.

with gas (and star) particle masses of $1.1 \times 10^6 M_{\odot}$. Two of these halos (15 and 18) would form massive galaxies at $z = 0$, and the third one (Scl54) would form a cluster. At $z = 2.95$ their virial masses are $4.2 \times 10^{11} M_{\odot}$, $3.0 \times 10^{11} M_{\odot}$ and $1.6 \times 10^{13} M_{\odot}$, respectively. In the latter proto-cluster run SF and feedback is modeled with a set of discrete star particles assuming a Salpeter IMF. One of the proto-galaxies (AY18) was modeled with a top-heavy Arimoto-Yoshii IMF, and the other proto-galaxy was rerun twice, once with the Salpeter (S15) and once with the Arimoto-Yoshii (AY15) IMFs, respectively. We then took these halos at $z = 2.95$ and projected them onto a hierarchy of nested grids with interpolated grid resolution of 45 pc for the two proto-galaxies and 150 pc for the proto-cluster. We postprocessed these datasets with the UVB radiative transfer using the same algorithm as for our grid-based simulations (Sec. 2.1), and with transfer of stellar ionizing photons using the adaptive ray splitting method described in Razoumov & Sommer-Larsen (2006). The stellar UV luminosity is determined using the population synthesis package Starburst 1999 (Leitherer et al. 1999) with continuous SF distributed among all stars younger than 34 Myrs.

Figure 9 shows the differential HI column density and cumulative v_{90} velocity width distributions for the four models. These distributions were computed with the ran-

dom sightlines passing through the resimulated volumes which have the average densities in excess of the mean density of the Universe at $z = 2.95$. Therefore we should expect more absorption than from a truly representative large cosmological volume, which is evident in the upper plot of Fig. 9. However, since these volumes contain massive environments, they should exhibit a higher neutral gas velocity dispersion than a larger cosmological volume. The median v_{90} velocity width for models S15, AY15, AY18, and Scl54 is 32, 34, 31, and 31 km s^{-1} , respectively. This is a surprising result, as with suppression of cooling in the feedback regions one would expect to see a more efficient conversion of feedback energy into hydrodynamical expansion and, therefore, higher outflow velocities. In fact, we see that increasing the strength of feedback has some effect on velocities. AY15 is the same proto-galaxy as S15, resimulated with the top-heavy Arimoto-Yoshii IMF with stronger feedback. Figure 9 shows that more energetic feedback removes gas from higher column densities and produces a larger fraction of high-velocity DLAs, although the median v_{90} changes only slightly from 32 to 34 km s^{-1} .

Note that our kinematics results are independent of the assumed UVB. Changing the amplitude and hardness of the UVB does not alleviate the lack of high-velocity systems, as it affects primarily lower column density absorbers, and since there is effectively no correlation between the velocity widths and column densities (lower panel of Fig. 4), changing the UVB just adds or removes both low- and high-velocity DLAs from the simulated sample.

4. DISCUSSION

We have performed a numerical study of DLA kinematics using high-resolution grid-based AMR simulations with moderate feedback, as well as particle-based SPH models with much more efficient feedback. With grid-based models our goal was to test the hypothesis that the observed velocity dispersion in DLAs could be explained by energy coming from gravitational collapse of cosmic structures. The broadest line profiles would then come from neutral clouds surviving infall into the massive virialized ($\gtrsim 10^{11} M_{\odot}$) systems, as a $10^{11} M_{\odot}$ halo at $z = 3$ has a circular velocity already in excess of 100 km s^{-1} . We used a series of models with a comoving volume size ranging from $4h^{-1}$ to $32h^{-1}$ Mpc and the maximum physical resolution of 100 pc to build a DLA population covering halos in the mass range $10^{8.5} - 10^{13} M_{\odot}$. Although our models can reproduce well the total incidence rate of DLAs at $z = 3$, our median v_{90} velocities are of order $40 - 50 \text{ km s}^{-1}$, well below the observed value of 90 km s^{-1} . We can point out three possibilities to resolve this discrepancy:

1. *More massive environments* – The velocity dispersion in individual clouds is a strong function of mass. Therefore, one could expect that including more massive halos through sampling of the rare density peaks could alleviate the velocity problem. On the other hand, all our 4-16 Mpc high resolution models feature similar velocity tails (Fig. 1) even though the mass function in the 16 Mpc model L1 extends to nearly 50 times more massive halos than in the 4 Mpc model N1. Therefore it seems unlikely that the more massive ($M_{\text{halo}} > 8 \times 10^{12} M_{\odot}$) and consequently much rarer halos could make any substantial

contribution to the overall statistics, even though each individual halo could have a velocity dispersion of several hundred km s^{-1} .

Note that including only massive halos in larger simulation volumes might produce $f(N, X)$ at low N_{HI} which is too small (Jedamzik & Prochaska 1998) or too large, depending on the technique. In our simulations neglecting low-mass halos can actually raise $f(N, X)$ at low column densities, as all the gas which would otherwise be pulled in by low-mass halos stays in extended filaments which sometimes can produce column densities $N_{\text{HI}} > 10^{20.3} \text{ cm}^{-2}$. On the other hand, our larger 32 Mpc models H0 and H1 do not have enough grid resolution to resolve these filaments, and hence produce small line densities $\ell_{\text{DLA}}(X)$.

2. *Resolution* – Our current simulations are already very expensive computationally as we refine adaptively everywhere in the volume, and the 128^3 base grid models have in practice 300^3 to 400^3 resolution elements. If we start from 256^3 or a larger base grid, many more halos will form drawing in a larger fraction of baryons at earlier redshifts, whereas inside individual galaxies we will start resolving clumpy interstellar gas. However, without running these simulations and sampling a large number of galaxies at higher resolution, it is impossible to predict reliably the effect on the velocity and column density distributions. In addition, higher resolution would allow us to better model propagation of supernova-driven winds in the clumpy interstellar gas.

The key question is the relative contribution of lower mass ($\lesssim 10^{10.5} M_{\odot}$) and more massive ($\gtrsim 10^{10.5} M_{\odot}$) halos. In our current models these two populations contribute about equally to the total “galactic” DLA column density (Fig. 2). It is possible that at higher resolution the relative contribution of the more massive halos might grow, as they will feature more numerous spatially separated components falling on the same line of sight, perhaps with neutral gas tidal tails and bridges, whereas isolated lower mass galaxies could become even more compact and pull the remaining cold neutral gas from extended filamentary structures decreasing its covering factor on the sky.

Unfortunately, the spatial distribution of absorbing clouds cannot be reconstructed from the observed line profiles in the velocity space, which would otherwise point to the minimum scale needed to resolve multi-component DLAs. Lopez et al. (2002) studied an almost dust free DLA at $z = 2.33$ featuring 14 resolved metal line components. They found very similar Z/Fe ratios of low-ionization species in all 14 components, suggesting that these components could originate in clouds physically located in a small region of space, perhaps much smaller than the resolution limit of our current simulations.

3. *Local microphysics* – The most intriguing possibility is that the observed velocity dispersion could arise as a result of feedback from SF. More efficient feedback could disrupt the highest column density absorbers ($N_{\text{HI}} \gtrsim 10^{21.5} \text{ cm}^{-2}$) in the lower panel of Fig. 4 creating a population of low N_{HI} systems with high velocity widths. With such a disruption mechanism put in by hand with the galactic wind model, Nagamine et al. (2007) saw efficient gas removal from lower-

mass ($\lesssim 10^{10} M_{\odot}$) halos and increased cross-sections in $\gtrsim 10^{11} M_{\odot}$ halos. In view of our results, a model in which more efficient feedback is obtained without resorting to the unphysical assumptions of kinematic winds and/or suppressing cooling in feedback regions would seem particularly compelling. The key challenge here is to come up with a model which describes dynamics of individual components of the multiphase ISM separately from each other, either resolving them explicitly, or using a subresolution model in which different components are advected differently on a grid. In these models supernova winds would channel most of their energy into the lower density regions between the star-forming clouds, whereas the clouds would be more likely to survive the disruptive effect of the winds.

In Section 3 we used TreeSPH models to test the effect that the suppression of cooling has on neutral gas kinematics. We found the median velocity widths v_{90} of only 31 to 34 km s⁻¹, even though that these models have been shown to expel gas efficiently from the star-forming regions at high redshifts and produce realistic galactic disks at $z = 0$. In our view, such low velocity dispersion could be explained by a number of factors.

A. Resolution – When numerical models do not resolve density inhomogeneities in the ISM, putting a certain amount of supernova feedback into the thermal energy of the gas and turning off cooling leads to an efficient conversion of this energy into the superwind expansion into a nearly uniform medium. However, the mass loading of the wind in a uniform medium is much larger than in a clumpy medium of the same average density, since in the latter case the wind will predominantly expand into the lower density voids between the clumps creating a high velocity outflow which will occasionally sweep chunks of neutral material off the edges of denser clouds. Clumps of gas entrained in winds are often observed in low-redshift outflows Rupke et al. (2005). On the other hand, at low resolution winds will displace most gas in the galaxy moving it to somewhat higher galactic radii, producing “puffy” galaxies with a relatively low velocity dispersion. This is exactly what we see in SPH simulations at 45 pc physical resolution. The expectation is that at higher resolution we should see multiphase outflows, with higher overall velocities in hot ionized gas, and numerous dense clouds giving rise to multi-component low-ionization absorption lines. Getting such galactic winds from first principles is notoriously difficult in numerical simulations. In this paper, we argue that the necessary condition for obtaining the correct DLA velocity dispersion is a separate dynamical treatment of different components of the multiphase interstellar medium at $z = 3$.

In addition to the resolution effects, two other factors could have affected our SPH results. Here we just mention these effects briefly, as clearly their study goes beyond the reach of this paper.

B. Mean redshift of feedback – A realistic population of galaxies at $z = 0$ can be obtained in cosmological simulations invoking early ($z \gtrsim 4-6$) episodes of star formation

with energetic feedback (Sommer-Larsen et al. 2003). In this scenario, the radial distribution of gas and its angular momentum arise as a cumulative result of successive episodes of star formation driving gas out of the galaxies. Other model parameters might result in similar star formation histories; not all parameters can be constrained uniquely from observations. One could speculate that a different star formation history, e.g. one featuring energetic feedback down to redshift $z \sim 3$, would produce a higher neutral hydrogen velocity dispersion at such a redshift. We note that from the spectra of $z \sim 3-4$ LBGs, outflow velocities of 300 – 400 km s⁻¹ are routinely inferred (e.g., Pettini et al. 2001; Shapley et al. 2003). Note, however, also that Laursen & Sommer-Larsen (2007) were able to match both the magnitude and radial fall-off of Ly α surface brightness of typical $z \sim 3$ galaxies, indicating that the spatial distribution of neutral hydrogen is correctly predicted by current SPH models.

C. AGN feedback – It is possible that the core of each massive galaxy hosts a supermassive black hole which might have shown an AGN-type activity at some time in the past. Neither grid-based nor particle-based simulations presented in this paper include feedback from AGNs which could have a profound impact on gas kinematics in host galaxies.

Feedback from star formation is generally thought to play an important role in galaxy evolution. If galactic winds give rise to the observed neutral gas kinematics in DLAs, the same winds should affect the column density distribution. In Paper I and in this paper, we have attempted to look at both distributions through large-scale, “blind-survey” models, in which we simulate cosmological volumes using aggressive grid refinement for all galaxies. However, these models are very expensive to compute, especially as we get closer to resolving the typical scales of the ISM. Perhaps, a more efficient approach is to combine these large-scale numerical surveys with simulations of the ISM in isolated galaxies, whether or not accounting for mergers and cosmic infall. Fortunately, there is sufficient amount of observational data which can be used to constrain these models. Combining traditional QSO-DLA data with a closer look at the high-redshift star-forming regions with GRB-DLAs and with emission line studies should allow us to learn a lot more about young proto-galaxies in coming years.

The authors are grateful to the anonymous referee for his/her careful reviewing and constructive comments. The AMR simulations were performed at the San Diego Supercomputer Center (SDSC). The TreeSPH simulations were performed on the SGI Itanium II facility provided by the Danish Center for Scientific Computing (DCSC). This research was supported by the DFG cluster of excellence “Origin and Structure of the Universe”. The Dark Cosmology Centre is funded by the DNRFF.

REFERENCES

- Binney, J. 1977, ApJ, 215, 483
 Birnboim, Y. & Dekel, A. 2003, MNRAS, 345, 349
 Bouché, N., Murphy, M. T., Péroux, C., Csabai, I., & Wild, V. 2006, MNRAS, 371, 495
 Cen, R. & Ostriker, J. 1992, ApJ, 393, 22
 Dekel, A. & Birnboim, Y. 2006, MNRAS, 368, 2
 Dekel, A. & Woo, J. 2003, MNRAS, 344, 1131
 Haehnelt, M. G., Steinmetz, M., & Rauch, M. 1998, ApJ, 495, 647

- Jedamzik, K. & Prochaska, J. X. 1998, MNRAS, 296
- Laursen, P. & Sommer-Larsen, J. 2007, ApJ, 657, L69
- Ledoux, C., Petitjean, P., Fynbo, J. P. U., Møller, P., & Srianand, R. 2006, A&A, 457, 71
- Leitherer, C., Schaerer, D., Goldader, J. D., Delgado, R. M. G., Robert, C., Kune, D. F., de Mello, D. F., Devost, D., & Heckman, T. M. 1999, ApJS, 123, 3
- Lopez, S., Reimers, D., D'Odorico, S., & Prochaska, J. X. 2002, A&A, 385, 778
- Madau, P., Haardt, F., & Rees, M. J. 1999, ApJ, 514, 648
- Maller, A. H., Prochaska, J. X., Somerville, R. S., & Primack, J. R. 2001, MNRAS, 326, 1475
- McDonald, P. & Miralda-Escudé, J. 1999, ApJ, 519, 486
- Murphy, M. T., Curran, S. J., Webb, J. K., Menager, H., & Zych, B. J. 2007, astro-ph/0701028
- Nagamine, K., Wolfe, A. M., Hernquist, L., & Springel, V. 2007, ApJ, 660, 945
- Nulsen, P. E. J., Barcons, X., & Fabian, A. C. 1998, MNRAS, 301, 168
- O'Meara, J. M., Prochaska, J. X., Burles, S., Prochter, G., Bernstein, R. A., & Burgess, K. M. 2007, ApJ, 656, 666
- Pettini, M., Shapley, A. E., Steidel, C. C., Cuby, J.-G., Dickinson, M., Moorwood, A. F. M., Adelberger, K. L., & Giavalisco, M. 2001, ApJ, 554, 981
- Prochaska, J. X., Chen, H.-W., Wolfe, A. M., Dessauges-Zavadsky, M., & Bloom, J. S. 2007, astro-ph/0703701
- Prochaska, J. X., Gawiser, E., Wolfe, A. M., Castro, S., & Djorgovski, S. G. 2003, ApJ, 595, L9
- Prochaska, J. X., Herbert-Fort, S., & Wolfe, A. M. 2005, ApJ, 635, 123
- Prochaska, J. X. & Wolfe, A. M. 1997, ApJ, 487, 73
- Razoumov, A. O. & Cardall, C. Y. 2005, MNRAS, 362, 1413
- Razoumov, A. O., Norman, M. L., Prochaska, J. X., & Wolfe, A. M. 2006, ApJ, 645, 55
- Razoumov, A. O. & Sommer-Larsen, J. 2006, ApJ, 651, L89
- Rupke, D. S., Veilleux, S., & Sanders, D. B. 2005, ApJS, 160, 115
- Schaye, J. 2004, ApJ, 609, 667
- Shapley, A. E., Steidel, C. C., Pettini, M., & Adelberger, K. L. 2003, ApJ, 588, 65
- Sommer-Larsen, J., Götz, M., & Portinari, L. 2003, ApJ, 596, 47
- Springel, V. & Hernquist, L. 2003, MNRAS, 339, 289
- Stinson, G., Seth, A., Katz, N., Wadsley, J., Governato, F., & Quinn, T. 2006, MNRAS, 373, 1074
- Thacker, R. J. & Couchman, H. M. P. 2000, ApJ, 545, 728
- Tinker, J. L. & Chen, H.-W. 2007, astro-ph/0709.1470
- Wolfe, A. M. & Chen, H.-W. 2006, ApJ, 652, 981
- Wolfe, A. M. & Prochaska, J. X. 1998, ApJ, 494, L15
- Zwaan, M. A. & Prochaska, J. X. 2006, ApJ, 643, 675